remote sensing

MDPI

Article

Irrigation Events Detection over Intensively Irrigated Grassland Plots Using Sentinel-1 Data

Hassan Bazzi [1,*], Nicolas Baghdadi [1], Ibrahim Fayad [1], François Charron [2], Mehrez Zribi [3] and Hatem Belhouchette [4]

1 INRAE, UMR TETIS, University of Montpellier, AgroParisTech, 500 rue François Breton, CEDEX 5, 34093 Montpellier, France; nicolas.baghdadi@teledetection.fr (N.B.); ibrahim.fayad@inrae.fr (I.F.)
2 G-EAU Unit, University of Montpellier, AgroParisTech, CIRAD, INRAE, Institut Agro, IRD, Domaine du Merle, 13300 Salon de Provence, France; francois.charron@supagro.fr
3 CESBIO (CNRS/UPS/IRD/CNES/INRAE), 18 av. Edouard Belin, bpi 2801, CEDEX 9, 31401 Toulouse, France; mehrez.zribi@ird.fr
4 CIHEAM-IAMM, UMR-System, 34090 Montpellier, France; belhouchette@iamm.fr
* Correspondence: hassan.bazzi@inrae.fr; Tel.: +33-4-67-04-63-00

Received: 10 November 2020; Accepted: 9 December 2020; Published: 11 December 2020



Abstract: Better management of water consumption and irrigation schedule in irrigated agriculture is essential in order to save water resources, especially at regional scales and under changing climatic conditions. In the context of water management, the aim of this study is to monitor irrigation activities by detecting the irrigation episodes at plot scale using the Sentinel-1 (S1) C-band SAR (synthetic-aperture radar) time series over intensively irrigated grassland plots located in the Crau plain of southeast France. The method consisted of assessing the newly developed irrigation detection model (IDM) at plot scale over the irrigated grassland plots. First, four S1-SAR time series acquired from four different S1-SAR acquisitions (different S1 orbits), each at six-day revisit time, were obtained over the study site. Next, the IDM was applied at each available SAR image from each S1-SAR series to obtain an irrigation indicator at each SAR image (no, low, medium, or high irrigation possibility). Then, the irrigation indicators obtained at each image from each S1-SAR time series (four series) were added and combined by threshold value criteria to determine the existence or absence of an irrigation event. Finally, the performance of the IDM for irrigation detection was assessed by comparing the in situ recorded irrigation events at each plot and the detected irrigation events. The results show that using only the VV polarization, 82.4% of the in situ registered irrigation events are correctly detected with an F_score value reaching 73.8%. Less accuracy is obtained using only the VH polarization, where 79.9% of the in situ irrigation events are correctly detected with an F_score of 72.2%. The combined use of the VV and VH polarization showed that 74.1% of the irrigation events are detected with a higher F_score value of 76.4%. The analysis of the undetected irrigation events revealed that, in the presence of very well-developed vegetation cover (normalized difference of vegetation index (NDVI) $\geq$ 0.8); higher uncertainty in irrigation detection is observed, where 80% of the undetected events correspond to an NDVI value greater than 0.8. The results also showed that small-sized plots encounter more false irrigation detections than large-sized plots certainly because the pixel spacing of S1 data (10 m $\times$ 10 m) is not adapted to small size plots. The obtained results prove the efficiency of the S1 C-band data and the IDM for detecting irrigation events at the plot scale, which would help in improving the irrigation water management at large scales especially with availability and global coverage of the S1 product.

Keywords: irrigation; grassland; Sentinel-1; change detection; Crau plain; France

1. Introduction

In order to meet global food demand, which is affected by the global increase in the world population and climate change, current policies are pushing toward the expansion of the irrigated areas especially in arid and semi-arid regions [1–3]. According to the FAO (Food and Agriculture Organization of the United Nations), irrigated agriculture currently shares more than 40% of the global food production and accounts for approximately 70% of the total freshwater consumption considered thus the main consumer of freshwater [4]. Under limited water resources, efficient management of the irrigation schedule and timing is important to achieve the environmental sustainability in the agricultural sector [5]. In fact, obtaining information about irrigation timing is of great importance for several studies dealing with food security [6] and water consumption [7].

Satellite remote sensing has proven its high capability and effectiveness for mapping and monitoring irrigated areas [8–10]. Recent studies have shown that irrigated areas could be spatially quantified over large scale using either passive optical sensors [11–13] or active radar sensors [14–16]. Optical images has been widely used to map irrigated areas using the difference between the spectral signature of irrigated crops and that of non-irrigated crops in the time series domain. The difference in the temporal signal between irrigated and non-irrigated crop is based on the fact that irrigation mixed with fertilizers makes the crop grow healthier and faster causing a difference in the captured spectral signature between irrigated and non-irrigated plot. This difference in the spectral signature has been investigated using several vegetation indices such as the NDVI (normalized differential vegetation index) [17] or the GI (greenness index) [18]. On the other hand, the synthetic aperture radar (SAR) data has proven a superior efficiency over optical data for mapping irrigated areas [16,19,20]. The use of SAR data is mainly driven by the fact that the backscattered SAR signal is sensitive to the soil water content that is a key point in the irrigation activity [21–24]. Since irrigation increases the soil water content, the detection of irrigated areas could be possible using SAR data that are highly affected by the soil moisture values.

Although huge effort has been performed to quantify the extent and spatial distribution of irrigated areas, the timing and frequency of irrigation has not yet received important attention, despite their high importance in managing water resources. Using optical data, few studies have reported the detection of irrigation events. For example, Chen et al. [18] used MODIS (moderate resolution imaging spectroradiometer) and Landsat optical images with ancillary data (precipitation and soil moisture) to detect irrigation timing and frequency during the first half of the growing season. In their study, they performed a threshold-based model using the GI (greenness index) to count the possible water supplement stages. To distinguish between rainfall and irrigation events, which are both counted as water supplements, they used local daily precipitation records. Their results show that the overall accuracy of detecting a water supplement stage using the proposed method reaches 87%. However, the cloud limit could restrict the use of optical data despite the high revisit time of the new optical satellites such as the Sentinel-2 (S2) satellite that reaches 5 days.

On the other hand, SAR data could be used to detect the wetness information caused by irrigation episodes due to the sensitivity of the SAR backscattered signal to the soil water content [14–16,25]. However, the detection of irrigation by SAR data depends, in addition to the vegetation cover (crop type, density, growing phase, etc.), on the characteristics of the SAR satellite used (mainly revisit time and radar wavelength). The revisit time of the SAR satellite could constraint the detection of all the irrigation events due to the rapid drying out of the soil within few days after the irrigation. El Hajj et al. [26] showed that a radar image in X-band acquired 3 days after irrigation makes it difficult to certainly detect the irrigation event. This difficulty for detecting the irrigation event is due to the rapid dry out of the surface soil moisture which increases after an irrigation episode from 15–20 vol.% to reach 30–40 vol.%, and then the dries out three days after the irrigation event to reach the same value attained before irrigation (15–20 vol.%). Moreover, the used radar wavelength could constrain the detection of irrigation events. In fact, the available free and open access radar sensors provides C-band data (wavelength around 6 cm in the case of Sentinel-1). Recent studies [27] have

shown that the C-band SAR data could present certain limits for mapping soil moisture, due to the low penetration of the SAR signal over certain very well vegetation cover (case of irrigated maize). Moreover, El Hajj et al. [27] and Nasrallah et al. [28] showed that the sensitivity of the C-band SAR signal to soil moisture becomes negligible over wheat crops between the germination and the heading growing phases due to the low penetration of the C-band signal to the soil surface. Therefore, it is sometimes difficult to detect an increase in the radar signal due to an irrigation event, because the soil contribution is very low. However, recent studies have started exploiting the potential of SAR data for detecting irrigation events at plot scale. Recently, Bazzi et al. [29] developed a decision tree-based model to detect irrigation events at plot scale using S1 C-band SAR data. The proposed model relies on separating irrigation events from rainfall events using rainfall information derived from grid scale (10 km × 10 km) SAR backscattering signal [30]. By applying their model on three regions with different climatic contexts, they report that irrigation events could be detected by SAR data independent of the studied geographic context. In their study, they achieved a success rate of 84% in detecting irrigation events. However, they recommend that dense SAR temporal series help detect more irrigation events at plot scale. Since irrigation is a dynamic activity, the six-days revisit time of the S1 satellite remains a constraint for the detection of all irrigation events at plots scale. For this reason, an extensive temporal dataset is still required for the detection of all irrigation events occurring at plot scale. In addition, over irrigated maize plots of southwest France, La page et al. [31] investigated the potential of the S^2MP (Sentinel-1/Sentinel-2-derived soil moisture product [24]) to detect irrigation events at plot scale. The S^2MP is a soil moisture estimation product mainly derived by coupling Sentinel-1 SAR data and Sentinel-2 optical data using the neural network [24,32]. They showed that irrigation timing was detected with a good accuracy reporting an F-score between 80% and 83% for all studied plots. A lower accuracy of 69% was obtained when the vegetation cover is well developed (NDVI > 0.7). However, the study was only performed over five irrigated maize plots, which is still not considered robust enough for an operational application.

In France, the agricultural water consumption reaches 4.8 billion m^3 of the total withdrawn water. Particularly in of southeast France, the Crau plain is well known irrigated agricultural region exploited mainly for hay production. It covers an area of 12,500 ha and produces 100,000 tons of hay each year. The plain is intensively irrigated area that uses mainly the gravity irrigation technique. Despite the low irrigation efficiency of gravity irrigation, which is estimated at 60–70% [33], this technique is still used over the Crau plain for four centuries. Several studies have been conducted over the Crau plain in order to estimate surface soil moisture and monitor the irrigated grassland plots using SAR data. Using the X-band SAR data from TerraSAR-X and COSMO-SkyMed satellites, El Hajj et al. [26] showed that it is possible to track gravity irrigation and soil moisture variations from SAR X-band images acquired at high spatial resolution. In their study, they showed that over the irrigated grassland plots, the penetration depth of the radar wave in the X-band was high, even for dense and high vegetation (vegetation height more than 1 m); especially using the HH polarization. Moreover, Baghdadi et al. [34] showed that using the C-band RADARSAT data in the HH polarization, the surface soil moisture over the irrigated grassland plots could be estimated with an accuracy of 6 vol.%. In addition, El Hajj et al. [35] showed that the use of X-band SAR measurements in HH polarization for soil moisture estimation over the irrigated grassland plots produces an estimation accuracy of 3.6 vol.% for NDVI values between 0.45 vol.% and 0.75 vol.%, and 6.1 vol.% for NDVI between 0.75 and 0.90.

In the context of water resource management, especially under changing climatic conditions, the objective of this paper is to monitor irrigation activities over irrigated grassland plots in the Crau plain of southeast France using Sentinel-1 SAR data. In this study, the irrigation detection model proposed by Bazzi et al. [29] has been adopted to detect irrigation events at grassland plots using all possible Sentinel-1 SAR acquisitions. Given the exact irrigation dates at 46 different grassland plots, the performance of the used model is assessed and the accuracy of irrigation event detection is reported. The capability of detecting irrigation events using S1-SAR data was evaluated as a function of the plot geometrical structure, the vegetation cover and the specific type of grass. While Section 2 presents

the study site and materials used, Section 3 describes the methodology. Section 4 presents the main obtained results, followed by a discussion in Section 5. Finally, Section 6 shows the main conclusions.

2. Materials

2.1. Study Site

In this study, forty-six intensively irrigated grassland plots located in the Crau Plain of Southeast France (N 43°38′; E 5°1′) were examined (Figure 1). The Crau plain has a Mediterranean climate characterized by mild winter and dry summer season. For the past 15 years, rainfall amounts are relatively variable between years and ranges between 350 and 800 mm. Figure 2 represents the daily rainfall and temperature records in 2019 registered over the nearest local meteorological station located in "Salon-de-Provence", six km away from the study site. According to the registered precipitation data, the cumulative rainfall amounts in 2019 reaches 580 mm. The minimum-recorded temperature is 5.9 °C on 24/01/2019, while the maximum-recorded temperature is 43.5 °C, occurring on 28/06/2019. The average temperature in the summer season (between June and September) reaches 31.6 °C, with a cumulative rainfall of 37 mm only. Due to high temperatures in the summer season, the evaporation rate reaches 10 mm/day. In the Crau plain, the source of water for irrigation originates from the Alps Mountains.

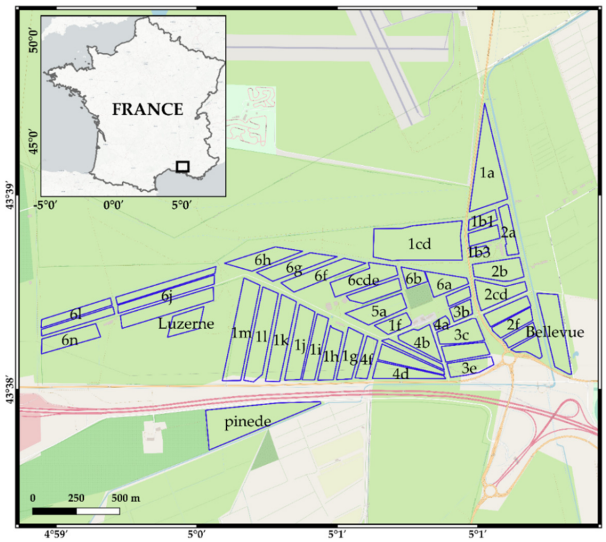


Figure 1. Location of the forty-six experimental plots in the Crau plain of Southeast France.

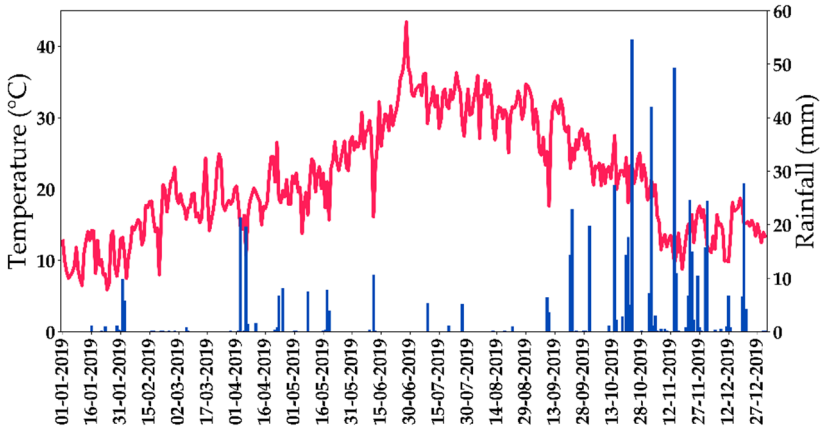


Figure 2. Temperature (in red) and rainfall (blue) profiles recorded at the local meteorological station in Salon de Provence near the study site.

2.2. Reference Data

The forty-six studied plots (Figure 1) are oriented toward hay production certified with the AOP French label (protected designation of origin), ensuring high quality of hay product [36]. Each plot undergoes three major cycles between February and September with three harvesting periods. The first cycle starts from the beginning of February until May with the first harvesting occurring in mid-May. The second cycle starts in May and is usually harvested in July which coincides with the beginning of the third cycle. The third cycle is finally harvested after mid-August. Different grass species are present in each plot with varying biomass proportions for each cycle. The 1st cycle is usually rich in grasses (60–65% of coarse hay). The grass percentage then decreases in the 2nd and 3rd cycles to reach 35% with the increase of the legumes proportion [36]. Therefore, the 1st cycle could be characterized as grass dominant cycle, whereas the second and the third cycle are legume dominant cycles (more leafy). Concerning the soil texture, loam is the dominant top soil texture among the plots, with depth varying between 30 and 80 cm. The area of the plots varies between 0.4 and 9.9 ha, with an average area of 2.8 ha.

Irrigation is performed using the gravity irrigation system where the gentle slope of the plots allows water to reach from the irrigation canals to cover the whole plot. The plots are usually irrigated between March and September of each year. The exact date of the end of each irrigation episode was registered at each plot for the period between March and September 2019. For each irrigation episode, the time between the start and the end of the irrigation usually varies between 1 and 24 h, depending on the surface of the plot [26]. Unfortunately, only the exact date of the end of irrigation was registered whereas the exact timing (in h) of the start and end of irrigation were not available. Some large surface plots are split into two different subplots being irrigated sequentially with a time difference of less than 24 h. In general, the average frequency of the irrigation for each grassland plot reaches one irrigation each 10 days during the three vegetation cycles with approximately 14 irrigation episodes per plot and a total water quantity between 15,000 to 20,000 m^3/ha. Finally, the mowing date for each cycle at each plot was also registered.

2.3. Sentinel-1 SAR Data

Over the study site, all available Sentinel-1 (S1) SAR images corresponding to the period between February 2019 and September 2019 were downloaded and processed. One hundred eighty C-band (f = 5.405 GHz) SAR images, acquired by the two polar-orbiting S1 satellites (S1A and S1B), were downloaded from the Copernicus website (https://scihub.copernicus.eu/dhus). The images are acquired in both ascending (afternoon ~18h00 UTC) and descending (morning ~06h00 UTC) modes. Each month, twenty images are available over the study site. Figure 3 shows the repeat cycle of the acquired S1 images in both ascending "A" and descending "D" modes for August 2019. The first image corresponds to the morning descending acquisition at an incidence angle of 32.2°. Twenty-four h later, another morning descending image is available at an incidence angle of 42.4°. A third image is then acquired twelve h later, corresponding to an afternoon ascending acquisition at 44.4° incidence angle. Finally, 24 h later, a new afternoon ascending image at 34.8° incidence angle is available. Thus, four S1 images are acquired within a period of 2.5 days. Since each one of the four acquisitions is repeated six days later (temporal resolution of S1 satellite), the time gap between the last afternoon acquisition and the first repeated morning acquisition is 3.5 days. Finally, four different temporal series were obtained where each temporal series represents the repeated images of the same acquisition mode each six days. The first series represents the 1st morning acquisition at incidence angle of 32.4° denoted by "MS1", while the second morning temporal series acquired at 42.4° is denoted by "MS2". The first afternoon SAR series at 44.4° is denoted by "AS1", while the second afternoon series at 34.8° is denoted by "AS2".

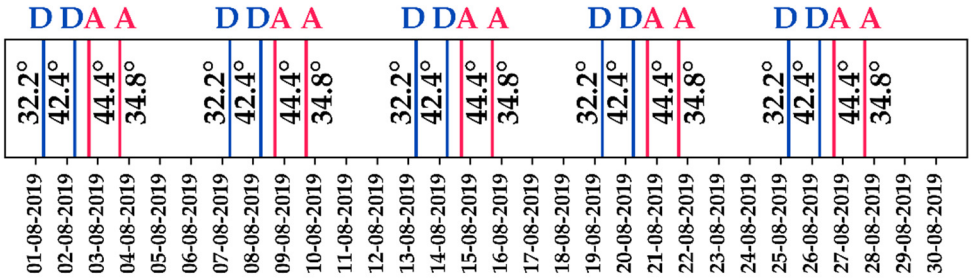


Figure 3. Repeat cycle of the Sentinel-1 images in ascending "A" (afternoon, red) and descending "D" (morning, blue) modes for the month of August 2019 over the examined plots.

To perform the radiometric and geometric calibration of the downloaded GRD SAR images, the S1 toolbox developed by the European Space Agency (ESA) was used. The radiometric calibration converts the digital number (DN) into backscattering coefficient (σ^0) expressed in linear unit. The geometric calibration uses the digital elevation model at 30 m spatial resolution, offered by the Shuttle Radar Topography Mission (SRTM), to ortho-rectify the SAR images.

2.4. Sentinel-2 Optical Data

The high temporal resolution of the Senintel-2 satellite (five days) allowed obtaining forty-six Sentinel-2 (S2) cloud free optical images acquired over the reference plots for the period between February and September 2019. The level-2 cloud free S2 images were downloaded from the Theia website (https://www.theia-land.fr/) which provides ortho-rectified level-2 products corrected for atmospheric effects. These optical images were used to calculate the NDVI values. The NDVI values are required as an input layer in the irrigation detection model used in this study [29].

3. Methods

3.1. Irrigation Detection Model

The irrigation detection model (IDM) was recently developed by Bazzi et al. [29] to detect irrigation events at agricultural plots in a near real-time scenario. The IDM is a decision tree-based model that relies on the change detection in the SAR backscattering coefficient at plot scale (σ^0_P) accompanied by the change detection of the SAR backscattering coefficient at grid scale (σ^0_G) of 10 km × 10 km. The joint use of σ^0_P and σ^0_G is mainly used to remove the uncertainty between a rainfall event and an irrigation event because both events are water supplements that cause an increase in soil moisture value and therefore an increase in σ^0 values between two dates. The IDM is based on detecting the change is σ^0_P values between the σ^0_P value at the current SAR acquisition at time t_i and σ^0_P value at the previous SAR acquisition at time t_{i-1}. Deep in details, the IDM assumes that the increase of the σ^0_P between two consecutive SAR dates (t_{i-1} and t_i) is mainly caused by the increase of the surface soil moisture due to either rainfall or irrigation event. On the other hand, the increase of the σ^0_G values (grid scale) could be an evidence of rainfall event that occurred between the two SAR acquisitions, whereas the stability or decrease of σ^0_G values could indicate the persistence of dry conditions between the two dates (absence of rainfall). Thus, the increase of the σ^0_P values between consecutive acquisitions accompanied with the stability or decrease of σ^0_G values is considered an irrigation event. Since the SAR backscattering signal could be affected by other factors, such as the vegetation cover (growth cycle for example) and surface roughness, additional filters considering the NDVI values and surface soil moisture estimations (SSM) are also added to the IDM to enhance the irrigation event detection. Therefore, the application of the IDM requires five principal data inputs:

- The SAR backscattering signal at plot σ^0_P and grid σ^0_G scales;
- Surface Soil Moisture at plot (SSM_P) and grid (SSM_G) scales;
- The NDVI value at plot scale.

3.1.1. σ° SAR Backscattering at Plot Scale

For each acquired S1 SAR image, the σ_P^0 at each of the forty-six plots was calculated by averaging the pixel values within each plot in both VV and VH polarizations. This average helps reducing the speckle filter present in the SAR images. As a result, four distinct temporal series are obtained for each plot using the four different SAR acquisitions discussed in Section 2.2 in both VV and VH polarizations. Although the study of Bazzi et al. [29] recommends the use of the VV polarization for better detection of irrigation events, the VH polarization was tested in order to assess the potential of VH polarization for detecting irrigation events. Moreover, the combined use of both VV and VH polarization for irrigation detection was also examined. The SAR incidence angle (θ_P) at each plot has been obtained for each SAR image.

3.1.2. σ° SAR Backscattering at Grid Scale

The σ_G^0 value at grid scale (10 km × 10km) was obtained at each SAR acquisition by averaging the SAR backscattering coefficient of all pixels corresponding to bare soil pixels or with small vegetation cover within each grid cell. Bare soil pixels with low vegetation cover has been extracted by using first a land cover map of France to delineate agricultural areas [37] and then applying a threshold value of the NDVI obtained from the S2 images (NDVI < 0.4). The σ_G^0 has been also obtained in both VV and VH polarizations as well as the average SAR incidence angle at each grid cell (θ_G) for each SAR image.

3.1.3. NDVI Values

The NDVI was calculated for the forty-six available S2 images. Then, the average NDVI value at each plot was obtained by averaging the pixels' values within each plot. The plot NDVI value is used as an input data layer for the IDM and used for estimating the SSM value at plot scale. In addition, at each grid cell, the average NDVI value was obtained for bare soil pixels with low vegetation cover, as discussed in Section 3.1.2, and used to obtain the SSM estimation at grid cell.

3.1.4. Surface Soil Moisture Estimation

The IDM requires the SSM estimation, as one of the input parameters, at each SAR acquisition for both plot and grid scales. As recommended by Bazzi et al. [29], the SSM estimations are derived using the neural network (NN) developed by El Hajj et al. [24]. This NN provides satisfying SSM estimations (RMSE = 5 vol.%) and needs as inputs the σ^0 value in VV polarization, the SAR incidence angle (θ) and an NDVI value. Therefore, the SSM estimations are obtained for each plot and for each grid cell at each available SAR date in the four temporal series MS1, MS2, AS1 and AS2. However, the soil moisture estimations do not have a major role in the irrigation detection. They are mostly used to ensure the detection of irrigation events in some cases where the difference of the SAR backscattering signal at plot scale could not lead to a definitive decision on the existence of irrigation events.

3.2. Application and Assessment of the IDM

Figure 4 represents the overflow of the IDM application at a given plot using four SAR temporal series. First, the IDM was applied at each plot using inputs from each SAR temporal series (MS1, MS2, AS1 and AS2) independently. For example, at time t_i in the MS1 series, irrigation detection using the IDM has been performed using only SAR images from the MS1 time series between t_0 and t_{i-1}. While developing the IDM, Bazzi et al. [26] proposed a certainty indicator, which represents the chance of having an irrigation event at each SAR date. This certainty indicator depends mostly on the observed difference of σ_P^0 between two consecutive SAR dates from the same temporal series. Therefore, at each plot, each SAR image from each series is labelled with an irrigation indicator value (p) that represents irrigation chances as either no ($p = 0$), low (25), medium (50) or high (100). In the IDM, the indicator value 0 represents either a decrease in the σ_P^0 between t_{i-1} and t_i ($\Delta\sigma_P^0 \leq 0$) indicating a decrease in soil moisture values (no irrigation possibility) or an important increase of the σ_G^0 ($\Delta\sigma_G^0 \geq 1$ dB) between t_{i-1}

and t_i indicating the presence of a rainfall event. Low irrigation chance indicator ($p = 25$) corresponds to a very slight increase in the σ^0_P between t_{i-1} and t_i ($0 \leq \Delta\sigma^0_P < 0.5$ dB) accompanied with high estimated soil moisture values at plot scale at t_i along with an important decrease of the σ^0_G at grid scale between t_{i-1} and t_i ($\Delta\sigma^0_G \leq 1$ dB), indicating the absence of a rainfall event. In this case, the SSM estimations at plot scale presented in Section 3.1.4 are used to guarantee the existence of an irrigation event. The stability or slight increase of the SAR signal at plot scale between t_i and t_{i-1} could be interpreted as an irrigation event (low chance) if the σ^0_P at time t_{i-1} already attains high values (due to irrigation or rainfall). To ensure this situation, we say that at time t_{i-1}, SSM estimation should be greater than or equals to 20 vol.% in order to guarantee that a humid soil conditions at time t_{i-1} have continued to time t_i. The medium chance index ($p = 50$) corresponds to a moderate increase in the σ^0_P between t_{i-1} and t_i ($0.5 \leq \Delta\sigma^0_P < 1$ dB) accompanied with a decrease of the σ^0_G ($\Delta\sigma^0_G \leq 0.5$ dB). Finally, high chance irrigation index ($p = 100$) corresponds to important increase in the σ^0_P between t_{i-1} and t_i ($\Delta\sigma^0_P \geq 1$ dB) accompanied with a decrease of the σ^0_G (increase of soil moisture at plot scale at t_i with no rainfall event between t_{i-1} and t_i). Therefore, a value (p) equals to 100 represents the highest chance of existing irrigation. As the value of p decreases, the irrigation chance decreases to reach zero for no possible irrigation. As a result, the four SAR temporal series are transformed into labelled series of irrigation indicators showing the possibility of an existing irrigation event for each SAR date. It is good to mention that the irrigation indicator p is obtained at each SAR image using only the images from its corresponding SAR time series acquisition (orbit) at 6 days interval (Figure 4) where $(t_i - t_{i-1})$ $= (t_j - t_{j-1}) = (t_k - t_{k-1}) = (t_q - t_{q-1}) = 6$ days.

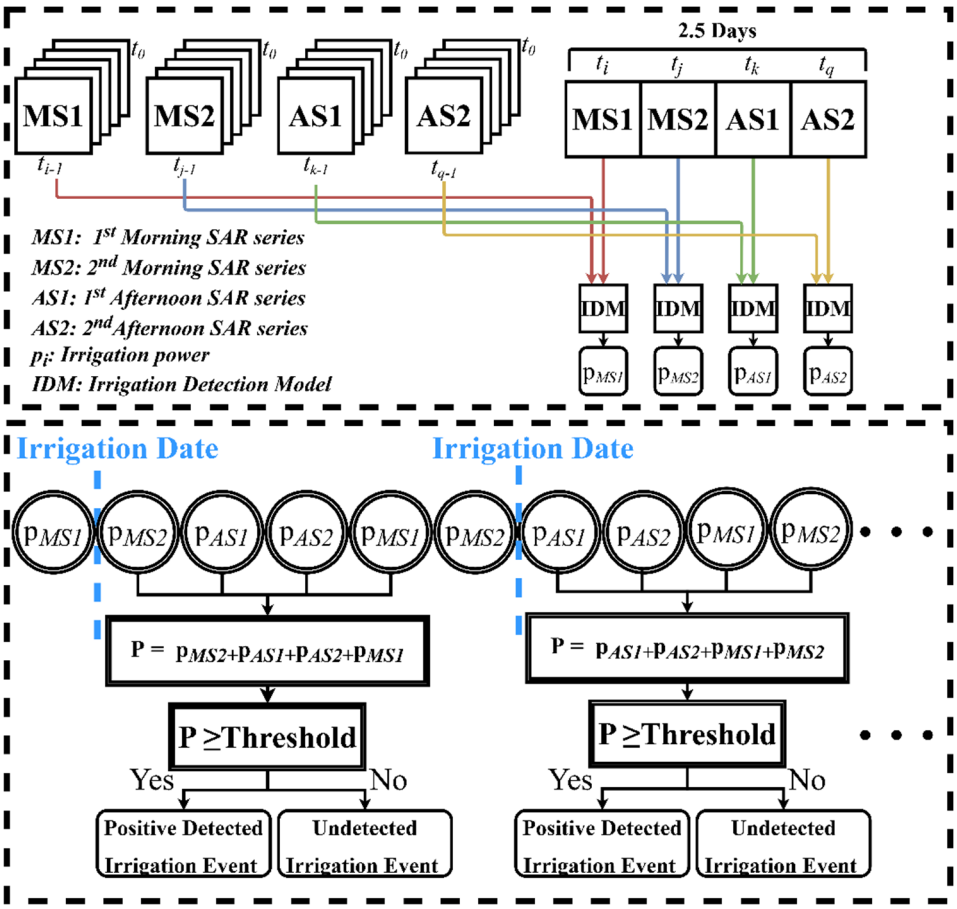


Figure 4. Overflow of the methodology for the detection of irrigation events using the irrigation detection model (IDM) and four synthetic aperture radar (SAR) temporal series. The time intervals $(t_i - t_{i-1})$, $(t_j - t_{j-1})$, $(t_k - t_{k-1})$, $(t_q - t_{q-1})$ are equal to 6 days.

The second step is to compare the obtained labelled SAR dates of the four SAR series with the irrigation dates registered for each plot. To compare between in situ irrigation events and detected irrigation events from the four SAR time series, the *p* indicators coming from the four series were combined and compared to a threshold value, to determine the detection or not of in situ irrigation event. For each in situ irrigation date, four irrigation "*p*" values (one indicator from each image following this event from the four SAR series) are available. The four *p* values correspond to the irrigation chances detected by each SAR image that follows this irrigation event. The four obtained *p* values are then summed to obtain a value (P) for this irrigation event. Finally, the obtained P value is compared to a threshold in order to determine if the irrigation has been positively detected (considered as a true detection) (Figure 4). Inversely, if an irrigation episode attains a P value less than the fixed threshold then the event is considered as undetected irrigation event. In this study, the threshold values of 25, 100, 150 and 200 are tested. Finally, false detections are detected irrigation events but actually, no irrigation event is registered on the plot. This means that the P value (obtained from four SAR image encountering the false detection) is greater than the determined threshold but no real irrigation event is registered.

The IDM was applied on the four SAR series using the VV and VH polarizations separately. The assessment of the IDM for irrigation detection was then performed in four different configurations. The first and the second configurations correspond to the application of the IDM using the VV and the VH polarizations, respectively. In the third configuration, "VV and VH", a detected event is considered as an irrigation event of the IDM if it is detected within both VV and VH configurations. Finally, in the fourth configuration "VV or VH", a detected event is considered as an irrigation event of the IDM if it exists within either the VV or VH the configurations. In the four configurations, the number of positively detected events, undetected events and the falsely detected events are registered.

Three accuracy metrics are calculated to assess the performance of the IDM for detecting irrigation events over grassland plots for each configuration. The first metric "S" is related to the sensitivity of the IDM for detecting irrigation events also known as the recall Equation (1). It reflects the ratio between the number of the positively detected irrigation events by the IDM and the total number of irrigation events on the plots. High S values represent the successful detection of irrigation events with low number of undetected events. The second metric "Pr" is the ratio between the positively detected irrigation events and all the detected events (true and false detections) by the IDM, also known as the precision Equation (2). High precision values mean that irrigation events are detected with low possibility of obtaining false detections (events detected as irrigation but no real irrigation events occur). To assess the performance of the model in detecting irrigation events, it is important to quantify simultaneously the number of irrigation events that could be positively detected represented by "S" and the additional false irrigations that could be detected represented by "Pr". In order to obtain a balanced quantification between the sensitivity and the precision, the F_score value is calculated by Equation (3). The F_score is the harmonic mean between the recall (S) and the precision (Pr) that allows the comparison of the global accuracy for irrigation detection between the several thresholds and configurations used. In this study, the three accuracy metrics were calculated on all the tested threshold values of P (25, 100, 150 and 200) and for each of the four configurations.

$$\mathrm{S} = \frac{\text{Number of Positive Detected Events}}{\text{Number of All Existing Irrigation Events}} \times 100\% \quad (1)$$

$$\mathrm{Pr} = \frac{\text{Number of Positive Detected Events}}{\text{Number of All Detected Events}} \times 100\% \quad (2)$$

$$\text{F_score} = \frac{2 \times \mathrm{S} \times \mathrm{Pr}}{\mathrm{S} + \mathrm{Pr}} \times 100\% \quad (3)$$

4. Results

4.1. Irrigation Detection Using VV and VH Separately

Table 1 summarizes the results obtained for the assessment of the irrigation detection using the IDM for the VV and the VH configurations separately. At each configuration, four threshold values of P were tested. The P value is obtained as a sum of the four p values from the four SAR images corresponding to each irrigation event. The p values are obtained in IDM for each SAR image using only its corresponding SAR time series (same orbit acquisition) at a 6 day time interval. The first tested threshold value ($P \geq 25$) means that an irrigation event is detected if it exists, at least, on one SAR image from the four SAR time series with any obtained irrigation chance (25, 50 or 100). This threshold ensures the positive detection of most of the existing irrigation events in both VV (82.4%) and VH (79.90 %), but with high chance of having false detections with Pr-value of 66.9% and 65.8% for VV and VH, respectively. The second tested threshold corresponds to $P \geq 100$. This threshold occurs if at least one of the four SAR images shows high irrigation chance ($p = 100$) or two out of the four images ensures a medium irrigation chance (2×50) or the four SAR images shows low irrigation probability simultaneously (4×25). Using the VV polarization, 66.5% of the events could be correctly detected with high detection precision of Pr-value reaching 81.6% (18.4% of false detection could be obtained). Using the VH polarization, 60.1% of the irrigation events could be detected with a precision of 76.8%, where the chance of having false detections reaches 23.2%. For the threshold value 150, an irrigation event should exist at least with high chance on one of the four images accompanied with medium chance on another image or low chance on two other images ($100 + 50$ or $100 + 2 \times 25$). This condition ($P \geq 150$) could be also attained if at least three out of the four images shows medium irrigation chance (3×50) or two images with medium chance and two images with low chance ($2 \times 50 + 2 \times 25$). In the case of $P \geq 150$, the sensitivity value "S" decreases since less events could satisfy the threshold values, but the precision increases indicating that less falsely detected irrigation events could be obtained. In fact, using the VV polarization, only 44.6% of the events could still be detected with $P \geq 150$, but with a high detection precision with Pr_value reaching 91.8% (only 8.2% of false detections could be obtained). For the VH polarization, only 29.7% of the irrigations could be detected with high precision value Pr reaching 86.6%. Finally, the threshold value $P \geq 200$ means that an irrigation could be detected if it exists at high chance on one image accompanied with either a high chance on another image ($100 + 100$) or two medium chances on two images ($100 + 2 \times 50$). It could also be satisfied if the four images show medium irrigation chances (4×50). For very high tested P value ($P \geq 200$), the sensitivity drops for S = 32.3% using the VV polarization and 18% using the VH polarization. This drop in the sensitivity value is expected since higher thresholds constraints the detection of irrigation and obliges an event to be present with high and medium chances of several images among the four SAR images.

Table 1. Accuracy metrics obtained for the assessment of the IDM for irrigation detection using VV and VH polarizations separately.

Configuration	Metric	Thresholds			
		$P \geq 25$	$P \geq 100$	$P \geq 150$	$P \geq 200$
VV	S (%)	82.4	66.5	44.6	32.3
	Pr (%)	66.9	81.6	91.8	93.7
	F_score (%)	73.8	73.3	60.0	48.0
VH	S (%)	79.9	60.10	29.7	18.0
	Pr (%)	65.8	76.8	86.6	85.44
	F_score (%)	72.2	67.4	44.2	29.7

Table 1 shows that low threshold values (i.e., $P \geq 25$) allow for the detectiog of most of the irrigation events (S equals to 79.9% and 82.4% for VH and VV respectively). However, this high detection is accompanied with moderate possibility of obtaining additional false detections where the

Pr values reaches 66.9% and 65.8% for VV and VH, respectively. On the other hand, high threshold values (i.e., $P \geq 200$) ensure a low chance of obtaining any false irrigation event with higher precision Pr reaching 93.7% in VV polarization. However, in this case only one-third of the irrigation events could be detected (32.3%).

Figure 5 represents the average sensitivity (S) (Figure 5a), precision (Pr) (Figure 5b) and F_score (Figure 5c) at each month in VV and VH polarizations for a P threshold value equals to 25. This threshold value was used since it represents the highest F_score value compared to the other tested thresholds in both VV and VH polarizations. Figure 5a shows that in both VV and VH polarizations, the lowest percentage of detected irrigations occurs during the first cycle (Cycle I) in March, April and May. Using VV, the S-value reached 69.0%, 60.0% and 60.5% for March, April and May, respectively. For VH polarization, a sensitivity of 64.2%, 58.4% and 57.1% for March, April and May is obtained, respectively. For Cycle I, the precision value Pr (Figure 5b) and F_score (Figure 5c) show low values for both VV and VH, indicating low precisions for irrigation detection with a high possibility of obtaining false detections. During the second cycle (Cycle II) and the third cycle (Cycle III), the percentage of truly detected irrigation events (S) increases for both VV and VH. In these two cycles the S value ranges between 91.5% (in June) and 96.2% (in August) for the VV polarization. For the VH polarization, the S-value ranges between 83.9% (in June) and 96.2% (in August). The precision value Pr also increases during Cycle II and Cycle III to reach its maximum value of 74.5% for the VV polarization in July and 78.8% for the VH polarization in August. Similarly, Figure 5c shows that the F_score increases for Cycle II and Cycle III to reach its maximum value of 84.5% in July for VV and 86.6% in August for VH.

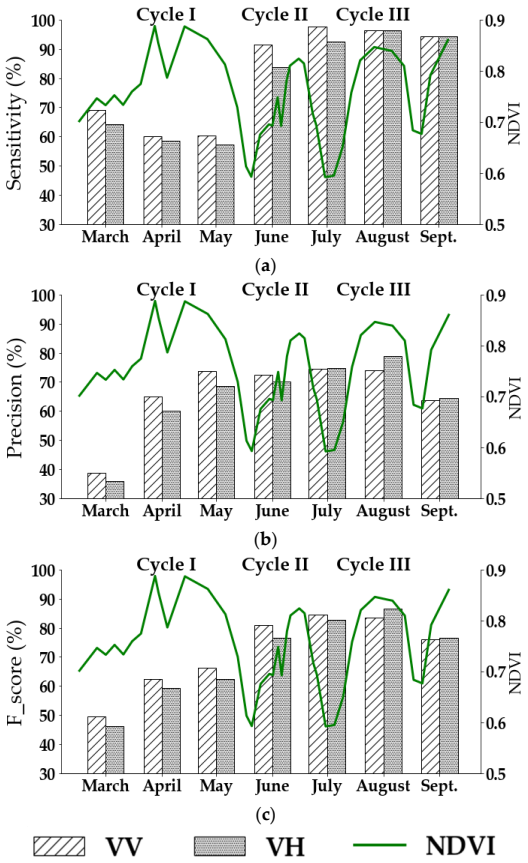


Figure 5. The accuracy of the detection of irrigation events in each month using the IDM for VV and VH over all the plots during the three vegetation cycles. (**a**) sensitivity "S", (**b**) precision "Pr" and (**c**) F_score. The green line represents the average normalized differential vegetation index (NDVI) values derived from S2 images for all the studied plots at the three distinct grass cycles.

4.2. Irrigation Detection Using Combined VV and VH

In this section, we report the combined use of both VV and VH polarizations for irrigation detection. As mentioned in Section 3.2, the results of irrigation detection using VV and VH were joined in two different configurations. The first configuration "VV or VH" implies that a detected event is considered an irrigation event if it is detected within either one of the VV or the VH polarizations or both. The second configuration "VV and VH" means that a detected event is registered as a detected irrigation event if it is present within both polarizations simultaneously. The obtained accuracy metrics are reported in Table 2.

Table 2. Accuracy metrics obtained for the assessment of the IDM for irrigation detection by the combined use of VV and VH in two different configurations.

Configuration	Metric	Thresholds			
		$P \geq 25$	$P \geq 100$	$P \geq 150$	$P \geq 200$
VV or VH	S (%)	88.2	76.8	51.6	38.0
	Pr (%)	58.5	72.8	87.4	89.5
	F_score (%)	70.3	74.7	64.9	53.3
VV and VH	S (%)	74.1	50.0	22.7	12.1
	Pr (%)	78.9	91.8	95.2	94.1
	F_score (%)	76.4	64.7	36.7	21.4

For low threshold value ($P \geq 25$), 88.2% of the total irrigation events (S) are detected in the "VV or VH" configuration with a moderate opportunity to obtain false detections with a precision (Pr) of 58.5% only. For the same value of P, the intersection configuration "VV and VH" shows less detection of irrigation events than "VV or VH" (S = 74.1%) but with higher precision (Pr = 78.9%) and, thus, a lower possibility of false detections compared to that obtained with "VV or VH" configuration. For $P \geq 100$, half of the irrigation events could be detected using the "VV and VH" configuration with high precision of 91.8% (only 8.2% of possible false detections). However, using the "VV or VH" configuration, 76.8% of the irrigation events are detected with a precision value reaching 72.8% indicating a 27.2% chance of having false detections. For higher threshold value ($P \geq 150$), half of the irrigation events (51.6%) could be detected using the "VV or VH" scenario with a precision of 87.4%. However, for the intersection configuration "VV and VH" the detection of irrigation events becomes difficult for $P \geq 150$, as the S value does not exceed 22.7% but with very high precision of 95.2%. Finally, with the threshold of 200, both configurations detect not more than 38% for "VV or VH" and 12.1% for "VV and VH" despite the high precision of 89.5% and 94.1%, respectively.

5. Discussion

In this section, the obtained results are analyzed as a function of group of factors that could limit the irrigation detection at plot scale. Among these factors, we consider the geometrical structure of the plot, the vegetation cover, the precipitation records and harvesting time of the plots. In order to discuss the obtained results, we chose the configuration attaining the highest F_score as the representative case for irrigation detection. The highest F_score has been chosen, since it represents the significant balance between the recall and the precision for the detection of irrigation events among the several tested thresholds and configurations. For this reason, the following discussion is based on the results obtained by the configuration "VV and VH" having a threshold value $P \geq 25$, which has the highest F_score of 76.4%, being a representative case for irrigation detection.

5.1. Effect of the Geometrical Structure of the Plots

The average σ^0_P calculated for all pixels within the plot could be affected by the geometrical shape of the plot. For example, narrow plots with very small width could have border pixels attaining the

backscattering values from the plot boundaries usually covered by trees, concrete or agricultural roads. Small plots as a function of width or length increases the chance of encountering speckle noise in the SAR backscattering coefficients, thus, causing undesirable fluctuation in the SAR signal (increase of σ_P^0 value). Therefore, one of the factors that could increase the possibility of encountering false detections is the geometrical structure of the plot such as the length, width and the surface area knowing that the Sentinel-1 images have pixel spacing of 10 m × 10 m. For this reason, we analyzed the false detections (events detected as irrigation where no registered irrigation exists) as a function of the length (l), width (w) and the surface area of the plots (S). For each plot the length, width and surface area have been calculated based on the RGF-93 projection system.

The grassland plots are generally elongated having a length significantly larger than the width (Figure 1). The length and width have been grouped into three classes to define small, average and large dimensional plots. The first class includes plots having a width less than 50 m or a length less than 150 m (10 plots). Independent of the first class, the second class contains averaged size plots having a width between 50 m and 100 m or a length between 150 m and 300 m (24 plots). Finally, the third class represents the large plots with a width more than 100 m and a length more than 300 m (12 plots). For each class, the average number of false detection is obtained by averaging the number of the false detections registered over all the plots in the class. Similarly, the surface area of the plots has been classified into three classes. The first class represents the plots with surface area less than 2 ha (18 plots), the second class contains plots with a surface area between 2 and 3 ha (17 plots), while the third class having the plots with a surface area more than 3 ha (11 plots). The average number of false detection is also obtained by averaging the number of the false detections registered over all the plots in the class.

Figure 6a represents the average false detections in each class as a function of the length-width grouping for the three classes and Figure 6b represents the average false detections as a function of the three surface area classes for "VV and VH" configuration with $P \geq 25$. Figure 6a shows that when the width (w) of the plot is narrow (less than 50m) or the length (l) is short (less than 150 m) the average false detections reaches five false detections per plot. The average false detections decreases to three false detections when the length (l) or the width (w) attains moderate sizes ($50 < w(m) < 100$ and $150 < l(m) < 300$). Finally, big plots that have wide width (greater than 150 m) and long length (greater than 300 m) encounters the least false detections having an average of one false detection per plot.

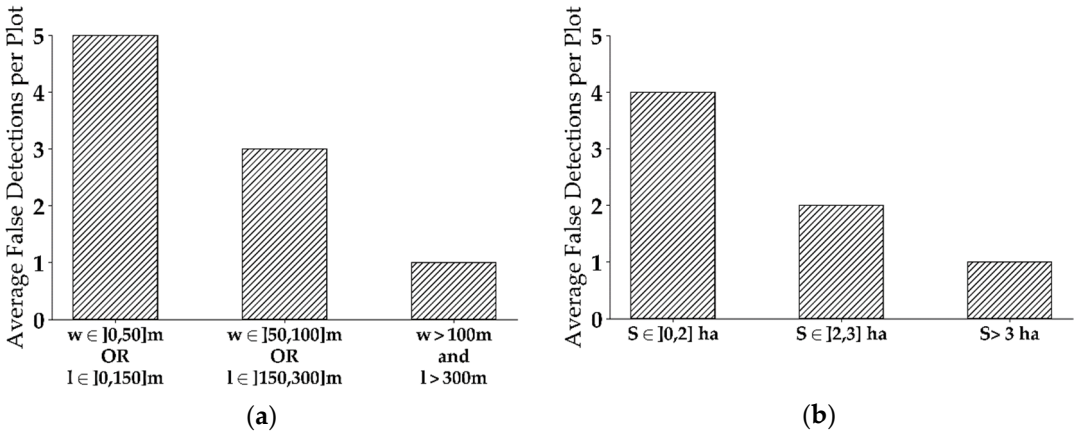


Figure 6. Average false detections per plot for each class as a function of (**a**) combined length-width and (**b**) surface area for "VV and VH" configuration with $P \geq 25$.

Similar results are shown by Figure 6b using the surface area. Small surface plots having an area less than 2 ha have the highest average false detections (an average of four false detections per plot). As the surface area increases, the average false detections decrease to reach an average of two false

detections per plot for medium surface area plots (between 2 and 3 ha) and an average of one false detection per plot for large surface area plots (greater than 3 ha).

5.2. Effect of the Vegetation Cover

The detection of irrigation events could be limited by the existing vegetation cover, depending on the crop type or the vegetation density. In fact, this limitation is mainly related to the ability of the SAR signal to penetrate the vegetation cover in order to reach the surface soil. El Hajj et al. [27] analyzed the penetration of the C-band SAR signal over maize, wheat and grassland plots. In their study, they showed that over grassland plots, the penetration of the C-band SAR signal is limited to an NDVI value of 0.7. They also showed that over highly developed grassland cover, the C-band signal is insensitive to the SSM. For this reason, very well-developed vegetation cover could constrain the detection of the irrigation events, due to the lack of the SAR sensitivity to surface soil moisture. Figure 7 represents the distribution of the NDVI values for the non-detected irrigation events over the forty-six plots. The figure shows that more than 80% of the undetected irrigation events correspond to very high NDVI values exceeding 0.8, and 90% of the undetected events correspond to NDVI greater than 0.7. These very high NDVI values indicate the presence of highly developed vegetation cover. These results are in line with the findings of El Hajj et al. [26] for grassland plots and La page et al. [31] for maize plots where both studies report the limitation of irrigation detection over dense vegetation cover (NDVI > 0.7) due to the limited penetration of C-band SAR signal.

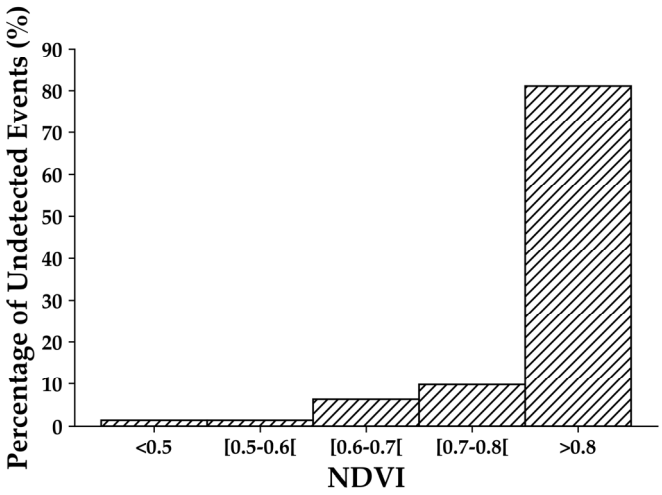


Figure 7. Distribution of the NDVI values for the non-detected irrigation events over all the plots among the three cycles for "VV and VH" configuration with $P \geq 25$.

As shown in Figure 5 in Section 4.1, the period with the least irrigation detection and highest false irrigation detection (in both VV and VH) corresponds to the first vegetation cycle from March to May, attaining the lowest sensitivity values compared to other months. In fact, independent of the NDVI values, the existing crop type could also affect the penetration of the SAR signal. As presented in Section 2.2, different grass types exist within the three cycles with different biomass proportion of each type. Actually, the grass type for the first cycle is more oriented toward coarse hay, which represents more than 65% of biomass in the existing vegetation cover of the first cycle. The vegetation cover in the first cycle is rich in grasses with less leaves and more stems [36]. With the stem elongation in March and April, the C-band SAR backscattering decreases due to the attenuation of the direct ground scattering. In fact, the vertical stems and leaves highly absorbs the incident SAR wave causing weak direct scattering of the SAR signal and thus a decrease in the C-band backscattering [27,38–40]. This attenuation behavior is also similar to that present on the wheat crop between the germination and the heading phase, as shown by Nasrallah et al. [28]. Therefore, for the period with very well developed vegetation cover for the first cycle, (NDVI > 0.8) the backscattering from the canopy (with

very low soil contribution) is the dominant mechanism, and the sensitivity of the SAR signal to the surface soil moisture is negligible. This high canopy attenuation of the soil contribution found in the first cycle is scarce in the second and the third cycles, since the grasses is less dominant, and the vegetation cover is leafier, containing more legumes than stems. In this case, the penetration of the C-band SAR signal is stronger and thus the soil contribution is more important. For this reason, higher accuracy in irrigation detection using the C-band SAR data is found for the second and third cycle than the first cycle (Figure 5).

To illustrate the vegetation attenuation mechanism that leads to the missing detection of irrigation events, Figure 8 presents a comparison between the backscattering SAR signal in VV polarization for the undetected irrigation events and that of the detected irrigation events for the four SAR temporal series MS1 (Figure 8a), MS2 (Figure 8b), AS1 (Figure 8c) and AS2 (Figure 8d). The boxplots in Figure 8 shows that within all the SAR acquisitions, the average σ^0 value of the undetected events is at least 2 dB less than the average σ^0 value for the detected events. For example, the median of the σ^0 for undetected events in MS1 at incidence angle of 32° (Figure 8a) reaches −13.1 dB, while that of the detected events reaches −10.8 dB, with a difference of 2.2 dB. Figure 8a also shows that approximately 75% of undetected events attains a σ^0 value less than the minimum σ^0 value of any detected irrigation event. Similar behavior is found for other SAR acquisitions at different incidence angles (Figure 8b–d). The low σ^0 values for the undetected events validates the existence of the high canopy attenuation mechanism that weakens the backscattered SAR signal (low soil penetration) and, thus, decreases the σ^0 values, indicating the absence of soil contribution in the SAR backscattered signal.

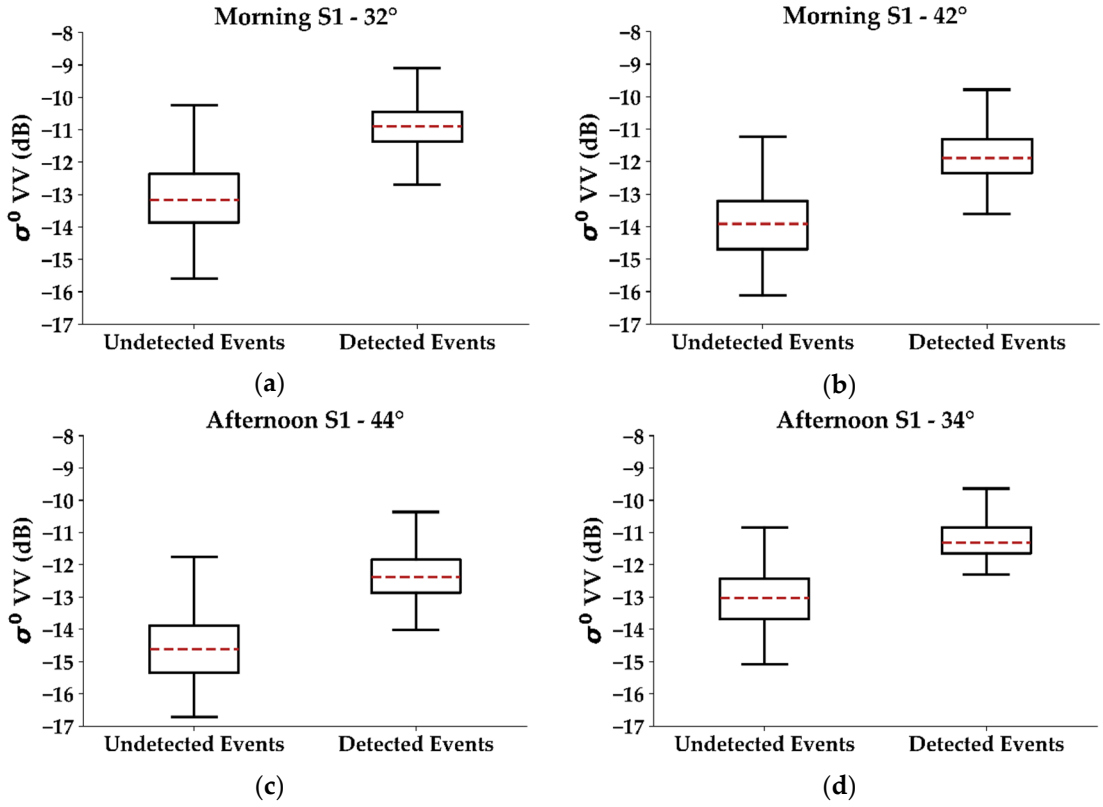


Figure 8. Boxplots of the distribution of σ^0-values in VV polarization for the detected and undetected events in the four temporal series. (**a**) MS1-32°, (**b**) MS2-42°, (**c**) AS1-44°, (**d**) AS2-34°.

5.3. Effect of Precipitation and Harvesting

In the Crau plain, the grassland plots are usually harvested three times per year, corresponding to the three existing cycles between March and September. The harvesting mechanism usually increases the surface roughness of the plot (Figure 9). In fact, the backscattered radar signal strongly depends

on the surface roughness that is usually expressed by the height root mean square (Hrms) [41]. Baghdadi et al. [42] reported that a difference of 4 dB could be observed between the backscattering signal from rough surfaces (Hrms = 3 cm) and smooth surface (Hrms = 0.5 cm). When the surface roughness increases between two consecutive SAR images due to harvesting, the backscattering SAR signal will increase between these two SAR dates and, thus, a false irrigation event could be detected. In this study, the harvesting date is available for each plot at each cycle. The comparison between the false detected irrigation events and the harvesting dates shows that 28% of the false detections were preceded by a harvesting activity. Therefore, a priori knowledge of the exact harvesting dates could help reduce the false detections.



Figure 9. Harvesting of a grassland plot with an increase in surface roughness.

Rainfall events can also limit the capability of detecting irrigation events. Certainly, when both a rainfall event and an irrigation event occurs between the same two consecutive SAR image, the irrigation detection would not be possible since the increase in the SSM values could not be distinguished between the rainfall event and the irrigation. Over the study site, five important rainfall events occurred on 03, 09 and 27 April and on 09 and 21 May. These rainfall events constrained the detection of 50 irrigation events over the forty-six plots, representing 20% of the total undetected events. The existence of rainfall events contributes also to the low sensitivity value of irrigation detection in March, April and May, shown in Figure 5a.

5.4. Sensitivity Analysis of the IDM $\Delta\sigma^0_P$ Threshold Values

In order to assess the effect of the threshold values fixed in the IDM for the detection of irrigation events, a sensitivity analysis has been performed on the threshold values of the main contributor in the IDM ($\Delta\sigma^0_P$) which is the difference between the SAR backscattered signal at plot scale between time t_i and time t_{i-1}. The threshold of $\Delta\sigma^0_P$ has been modified in order to analyze their impact on the results of the three indicators: sensitivity (S), precision (Pr) and the F_score. In this sensitivity study, we used the four following configurations (1) VV with P = 25, (2) VH with P = 25, (3) "VV and VH" with P = 25", and (4) "VV or VH" with P = 100, which correspond to the best configurations identified in this study for the detection of irrigation events.

Two tests were carried out in the sensitivity analysis. The first test consists of adding 0.25 dB to the different threshold values considered for $\Delta\sigma^0_P$ in the irrigation events detection. This means that for low irrigation chances (p = 25), a new threshold of $\Delta\sigma^0_P$ between 0.25 dB and 0.75 dB are used instead of the initial threshold values between 0 and 0.5 dB. For the medium irrigation chances (p = 50),

the threshold values of $\Delta\sigma_P^0$ between 0.75 and 1.25 dB are newly used instead of the initial thresholds between 0.5 dB and 1 dB. Finally, for high irrigation chances (p = 100), a threshold value of $\Delta\sigma_P^0$ greater than 1.25 dB is used instead of the initial 1 dB value. The second test consists of adding 0.5 dB to the initial threshold values of the $\Delta\sigma_P^0$ making, thus, low irrigation chances (p = 25) with a threshold of $0.5 \leq \Delta\sigma_P^0 < 1$ dB, the medium irrigation chances (p = 50) with a threshold value $1 \leq \Delta\sigma_P^0 < 1.5$ dB, and the high irrigation chances (p = 100) with threshold values $\Delta\sigma_P^0 \geq 1.5$ dB.

Figure 10 shows the variation of the three accuracy metrics (S, Pr and F_score) as a function of the two-tested increase in the threshold values in the four configurations. The results show that, by increasing the threshold values, the sensitivity decreases (less event irrigation is detected) while the precision increases (less false detections could be obtained). Similarly, the F-score also decreases. For the case of VV (P = 25), the sensitivity decreases from 82.4% to 72.8% by adding 0.25 dB to the threshold values of $\Delta\sigma_P^0$ and to 69.9% by adding 0.5 dB to the thresholds. Thus, nearly 12% of the event irrigations initially detected with our starting thresholds will no longer be detected by increasing the values of the starting thresholds by 0.25 dB or 0.5 dB. For the same case, the precision increases from 66.9% with our starting thresholds to 74.3% by increasing the thresholds by 0.25 dB and to 76.4% by increasing the thresholds by 0.5 dB. Thus, the precision on the detection of irrigation events increases by approximately 10% by increasing the values of the starting thresholds by 0.25 dB or 0.5 dB. The effect of the increasing of the threshold values of $\Delta\sigma_P^0$ is clearly a decrease in the sensitivity when the precision increases and vice versa. What is also observed is that the sensitivity decreases more strongly than precision when the threshold value is increased. For example, for the configuration using VV and VH with P = 25, S decreases by 17.9% when the thresholds are increased by 0.5 dB, and Pr increases only by 8.3% when the thresholds are increased by 0.5 dB.

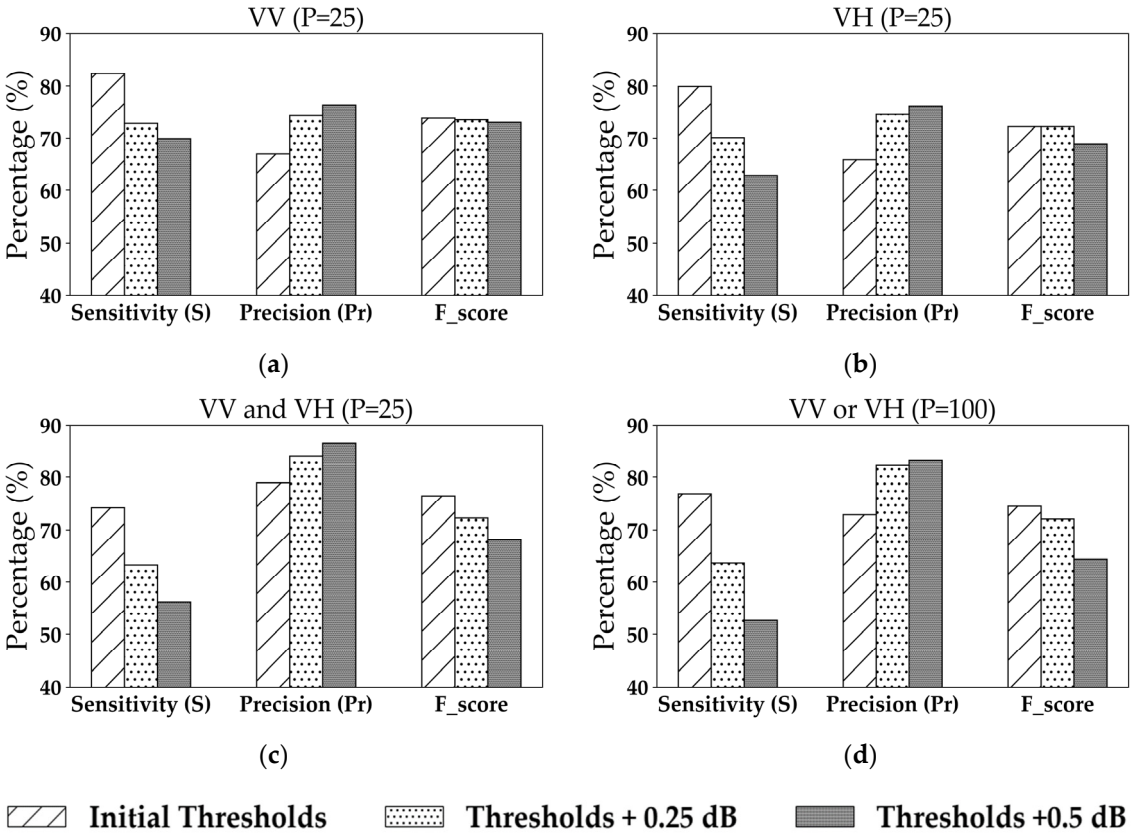


Figure 10. Variation of the accuracy metrics as a function of varying threshold values of $\Delta\sigma_P^0$ for (**a**) VV (P = 25), (**b**) VH (P = 25), (**c**) 'VV and VH' (P = 25) and (**d**) 'VV or VH' (P = 100).

5.5. Effect of the S1 Revisit Time on the Irrigation Detection

To study the effect of the S1 revisit time for the detection of irrigation events, a sensitivity analysis of the irrigation events detection as a function of the time lapse between the acquisition date of the S1 image and the irrigation date was performed. First, for each in situ irrigation event, we obtained the difference in days $\left(\Delta t = t_{S1} - t_{irrigation}\right)$ between the acquisition date of S1 images used for the detection in each of the four temporal series (MS1, MS2, AS1 and AS2) and the date of the irrigation event. Since the revisit time of the S1 is 6 days, the values of Δt for an irrigation event varies between 0 days (irrigation occurred the same date as the S1 passage) and 5 days (the SAR image was acquired 5 days after the irrigation event). At each value of Δt (0, 1, 2, 3, 4, 5) we obtained the total number of irrigation events and then we calculate the percentage of the detected events and the percentage of the undetected events by the IDM. Since the vegetation cover can also play an important role in the detection of irrigation events, we analyzed the percentage of detected and undetected irrigation events at each Δt value for two classes of NDVI values: (1) NDVI ≤ 0.7 and (2) NDVI > 0.7.

Figure 11 shows the percentage of detected and undetected irrigation events for each value of Δt between 0 and 5 days for NDVI ≤ 0.7 (Figure 11a) and NDVI > 0.7 (Figure 11b). For NDVI ≤ 0.7, the results show that if the S1 image is acquired at the same day of the irrigation event or one day after the irrigation event, we are able to detect approximately 75% of the irrigation events (Figure 11a). Two and three days after the irrigation event, the percentage of the detected and the undetected events are approximately the same (50%). Beyond 4 days of the irrigation event ($4 \leq \Delta t \leq 5$ days), the percentage of the detected irrigation events decreases. However, the percentage of undetected events increases and becomes greater than that of the detected events (60% and 40%, respectively).

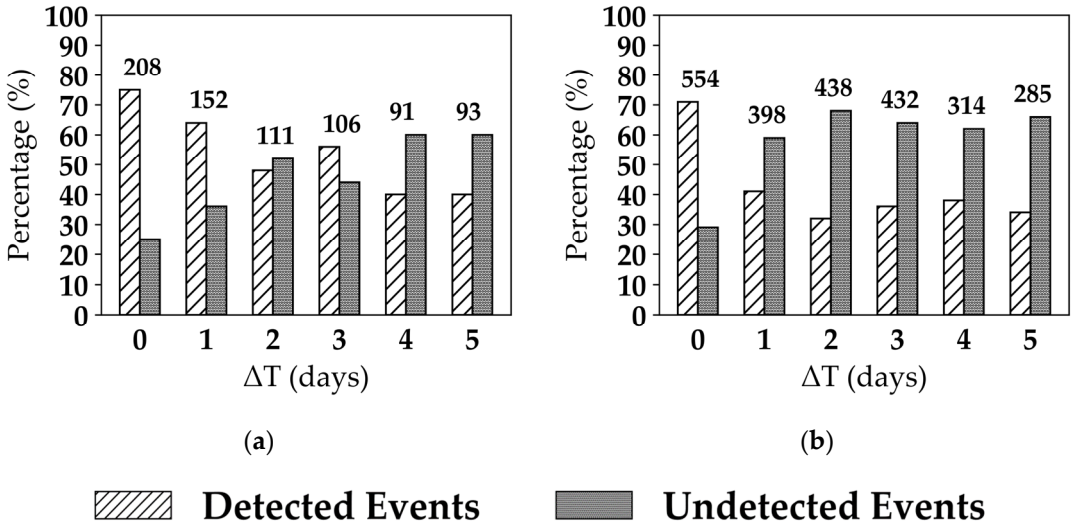


Figure 11. Percentage of detected and undetected irrigation events as a function of time laps between the S1 acquisition date and the irrigation date (Δt) for (**a**) NDVI ≤ 0.7 and (**b**) NDVI > 0.7. Numbers over the bars present the number of irrigation events at each value of Δt.

For NDVI > 0.7 (Figure 11b), 70% of the irrigation events could still be detected when the S1 image is acquired at the same date of the irrigation event ($\Delta t = 0$), whereas 30% of the events are not detected. These results are similar to that obtained for NDVI ≤ 0.7 and $\Delta t = 0$. However, one day after the irrigation event, the percentage of undetected events (60%) becomes greater than that of the detected events (40%). In the case where NDVI > 0.7, the percentages of detected and undetected events remain approximately stable for the values of Δt greater than 1 day (Δt equals to 2, 3, 4 or 5 days), with a percentage of undetected events greater than that of the detected events (60–70% and 30–40%, respectively).

6. Conclusions

In this study, the potential of the Sentinel-1 C-band time series for detecting irrigation events has been evaluated over intensively irrigated grassland plots located in the Crau plain of southeast France. The irrigation event detection has been carried out using the newly developed near real-time irrigation detection model (IDM). Four SAR time series from four different S1 orbits were used in this study. The IDM was first applied on each SAR time series of the same orbit acquisition (at a 6 day interval) to obtain irrigation indicators (low, medium and high irrigation chance) at each SAR image. Then, the irrigation indicators obtained at each image of the four SAR time series were combined and compared to a threshold value to obtain detected irrigation events.

The application of the IDM over all possible S1 SAR images in ascending and descending modes proved the capability of detecting irrigation events with a good accuracy. The results of the comparison between the in situ registered irrigation events and the detected irrigation events by the IDM showed that using the VV polarization the accuracy for irrigation detection reaches 73.8% by the means of F_score. The use of the VH polarization seems to be slightly less accurate than the VV polarization, with an F_score reaching 72.2%. However, the combined used of the VV and VH polarization enhances the irrigation detection accuracy to obtain an F_score of 76.4%. The analysis of the threshold value used for combining the irrigation indicators from all possible SAR acquisitions showed that the use of low threshold value allows higher detection of existing irrigation events with a sensitivity (S) of 74.1%, but with slightly high possibility of obtaining false detections where the precision (Pr) reaches 78.9% (the case of "VV and VH"). On the other hand, using high threshold values for combining the irrigation indicators from the four SAR time series, less irrigation events could be detected (S = 50%), but with higher precision and low chance of obtaining false irrigation detection with a high precision value of 91.8% (the case of "VV and VH").

The analysis of the undetected irrigation events as a function of vegetation cover and NDVI values showed that over leafy grass type (coarse hay) with very high NDVI values (NDVI > 0.8) the irrigation detection becomes difficult, due to the very low sensitivity of the C-band SAR signal to the surface soil moisture. The analysis of the falsely detected irrigation events, as a function of the plot size, showed that small sized plots in terms of narrow width or short length, (surface area less than 2 ha) encounter more false detections than large sized plots (surface area more than 3 ha), mainly due to the 10 m × 10 m pixel spacing of the S1 satellite. The analysis of the irrigation detection as a function of the time laps between the S1 acquisition and the irrigation date showed that for NDVI values less than 0.7, the irrigation event could be detected until two to three days after the irrigation event. However, for NDVI values greater than 0.7 the irrigation could only be detected if it exists within the same day of the S1 acquisition.

The obtained results present a quantitative evaluation of the capability of S1 data to detect irrigation events, which opens the way towards the operational use of the S1 data with the IDM to detect irrigation events over regional scales. The operational detection of irrigation events is ensured with the free and open access availability of the S1 data and the direct use of the IDM that does not require priori calibration (training) phase.

Author Contributions: Conceptualization, H.B. (Hassan Bazzi) and N.B.; Data curation, H.B. (Hassan Bazzi) and F.C.; Formal analysis, H.B. (Hassan Bazzi), N.B. and I.F.; Investigation, H.B. (Hassan Bazzi), N.B. and F.C.; Methodology, H.B. (Hassan Bazzi), N.B. and I.F.; Software, H.B. (Hassan Bazzi); Validation, H.B. (Hassan Bazzi), N.B., I.F., F.C., M.Z. and H.B. (Hatem Belhouchette); Visualization, H.B. (Hassan Bazzi); Writing—original draft, H.B. (Hassan Bazzi); Writing—review & editing, N.B., I.F., F.C., M.Z. and H.B. (Hatem Belhouchette). All authors have read and agreed to the published version of the manuscript.

Funding: This research received funding from the French Space Study Center (CNES, TOSCA 2020 project), the National Research Institute for Agriculture, Food and the Environment (INRAE), the Occitanie region of France and the Mediterranean Agronomic Institute of Montpellier (CIHEAM-IAMM).

Acknowledgments: Authors wish to thank the French Space Study Center (CNES, TOSCA 2020), the National Research Institute for Agriculture, Food and Environment (INRAE) and the Mediterranean Agronomic Institute of Montpellier (CIHEAM, IAMM). The authors wish to thank the Occitanie region, France for supporting this work.

The authors wish also to thank the European Space Agency (ESA) for the Sentinel 1 and Sentinel 2 data and Theia pole for the calibration of the Sentinel-2 images. The authors finally wish to thank Antoine Naudet from the Crau Hay Committee.

Conflicts of Interest: The authors declare no conflict of interest.

References

1. Tilman, D.; Clark, M. Food, agriculture & the environment: Can we feed the world & save the earth? *Daedalus* **2015**, *144*, 8–23. [CrossRef]
2. Tilman, D.; Balzer, C.; Hill, J.; Befort, B.L. Global food demand and the sustainable intensification of agriculture. *Proc. Natl. Acad. Sci. USA* **2011**, *108*, 20260–20264. [CrossRef] [PubMed]
3. Godfray, H.C.J.; Beddington, J.R.; Crute, I.R.; Haddad, L.; Lawrence, D.; Muir, J.F.; Pretty, J.; Robinson, S.; Thomas, S.M.; Toulmin, C. Food security: The challenge of feeding 9 billion people. *Science* **2010**, *327*, 812–818. [CrossRef] [PubMed]
4. Pokhrel, Y.N.; Hanasaki, N.; Wada, Y.; Kim, H. Recent progresses in incorporating human land-water management into global land surface models toward their integration into Earth system models: Recent progresses in incorporating human land-water management into global land surface models. *WIREs Water* **2016**, *3*, 548–574. [CrossRef]
5. Ozdogan, M. Exploring the potential contribution of irrigation to global agricultural primary productivity: Irrigation and Primary Productivity. *Glob. Biogeochem. Cycles* **2011**, *25*. [CrossRef]
6. Burney, J.; Woltering, L.; Burke, M.; Naylor, R.; Pasternak, D. Solar-powered drip irrigation enhances food security in the Sudano–Sahel. *Proc. Natl. Acad. Sci. USA* **2010**, *107*, 1848–1853. [CrossRef]
7. Paredes, P.; Rodrigues, G.C.; Alves, I.; Pereira, L.S. Partitioning evapotranspiration, yield prediction and economic returns of maize under various irrigation management strategies. *Agric. Water Manag.* **2014**, *135*, 27–39. [CrossRef]
8. Thenkabail, P.S.; Schull, M.; Turral, H. Ganges and Indus river basin land use/land cover (LULC) and irrigated area mapping using continuous streams of MODIS data. *Remote Sens. Environ.* **2005**, *95*, 317–341. [CrossRef]
9. Thenkabail, P.S.; Biradar, C.M.; Noojipady, P.; Dheeravath, V.; Li, Y.; Velpuri, M.; Gumma, M.; Gangalakunta, O.R.P.; Turral, H.; Cai, X.; et al. Global irrigated area map (GIAM), derived from remote sensing, for the end of the last millennium. *Int. J. Remote Sens.* **2009**, *30*, 3679–3733. [CrossRef]
10. Thenkabail, P.; Dheeravath, V.; Biradar, C.; Gangalakunta, O.R.; Noojipady, P.; Gurappa, C.; Velpuri, M.; Gumma, M.; Li, Y. Irrigated area maps and statistics of India using remote sensing and national statistics. *Remote Sens.* **2009**, *1*, 50–67. [CrossRef]
11. Dheeravath, V.; Thenkabail, P.S.; Chandrakantha, G.; Noojipady, P.; Reddy, G.P.O.; Biradar, C.M.; Gumma, M.K.; Velpuri, M. Irrigated areas of India derived using MODIS 500 m time series for the years 2001–2003. *ISPRS J. Photogramm. Remote Sens.* **2010**, *65*, 42–59. [CrossRef]
12. Gumma, M.K.; Thenkabail, P.S.; Hideto, F.; Nelson, A.; Dheeravath, V.; Busia, D.; Rala, A. Mapping irrigated areas of Ghana using fusion of 30 m and 250 m resolution remote-sensing data. *Remote Sens.* **2011**, *3*, 816–835. [CrossRef]
13. Xiang, K.; Ma, M.; Liu, W.; Dong, J.; Zhu, X.; Yuan, W. Mapping irrigated areas of northeast China in comparison to natural vegetation. *Remote Sens.* **2019**, *11*, 825. [CrossRef]
14. Gao, Q.; Zribi, M.; Escorihuela, M.; Baghdadi, N.; Segui, P. Irrigation mapping using sentinel-1 time series at field scale. *Remote Sens.* **2018**, *10*, 1495. [CrossRef]
15. Bousbih, S.; Zribi, M.; El Hajj, M.; Baghdadi, N.; Lili-Chabaane, Z.; Gao, Q.; Fanise, P. Soil moisture and irrigation mapping in a semi-arid region, based on the synergetic use of sentinel-1 and sentinel-2 data. *Remote Sens.* **2018**, *10*, 1953. [CrossRef]
16. Bazzi, H.; Baghdadi, N.; Ienco, D.; El Hajj, M.; Zribi, M.; Belhouchette, H.; Escorihuela, M.J.; Demarez, V. Mapping irrigated areas using sentinel-1 time series in Catalonia, Spain. *Remote Sens.* **2019**, *11*, 1836. [CrossRef]
17. Pervez, M.S.; Brown, J.F. Mapping irrigated lands at 250-m scale by merging MODIS data and national agricultural statistics. *Remote Sens.* **2010**, *2*, 2388–2412. [CrossRef]
18. Chen, Y.; Lu, D.; Luo, L.; Pokhrel, Y.; Deb, K.; Huang, J.; Ran, Y. Detecting irrigation extent, frequency, and timing in a heterogeneous arid agricultural region using MODIS time series, Landsat imagery, and ancillary data. *Remote Sens. Environ.* **2018**, *204*, 197–211. [CrossRef]

19. Bazzi, H.; Baghdadi, N.; El Hajj, M.; Zribi, M.; Minh, D.H.T.; Ndikumana, E.; Courault, D.; Belhouchette, H. Mapping paddy rice using sentinel-1 SAR time series in Camargue, France. *Remote Sens.* **2019**, *11*, 887. [CrossRef]
20. Fieuzal, R.; Duchemin, B.; Jarlan, L.; Zribi, M.; Baup, F.; Merlin, O.; Hagolle, O.; Garatuza-Payan, J. Combined use of optical and radar satellite data for the monitoring of irrigation and soil moisture of wheat crops. *Hydrol. Earth Syst. Sci.* **2011**, *15*, 1117. [CrossRef]
21. Baghdadi, N.; Choker, M.; Zribi, M.; Hajj, M.E.; Paloscia, S.; Verhoest, N.E.; Lievens, H.; Baup, F.; Mattia, F. A new empirical model for radar scattering from bare soil surfaces. *Remote Sens.* **2016**, *8*, 920. [CrossRef]
22. Aubert, M.; Baghdadi, N.N.; Zribi, M.; Ose, K.; El Hajj, M.; Vaudour, E.; Gonzalez-Sosa, E. Toward an operational bare soil moisture mapping using TerraSAR-X data acquired over agricultural areas. *IEEE J. Sel. Top. Appl. Earth Obs. Remote Sens.* **2012**, *6*, 900–916. [CrossRef]
23. Baghdadi, N.; Camus, P.; Beaugendre, N.; Issa, O.M.; Zribi, M.; Desprats, J.F.; Rajot, J.L.; Abdallah, C.; Sannier, C. Estimating surface soil moisture from TerraSAR-X data over two small catchments in the Sahelian Part of Western Niger. *Remote Sens.* **2011**, *3*, 1266–1283. [CrossRef]
24. El Hajj, M.; Baghdadi, N.; Zribi, M.; Bazzi, H. Synergic use of sentinel-1 and sentinel-2 Images for operational soil moisture mapping at high spatial resolution over agricultural areas. *Remote Sens.* **2017**, *9*, 1292. [CrossRef]
25. Bousbih, S.; Zribi, M.; Lili-Chabaane, Z.; Baghdadi, N.; El Hajj, M.; Gao, Q.; Mougenot, B. Potential of sentinel-1 radar data for the assessment of soil and cereal cover parameters. *Sensors* **2017**, *17*, 2617. [CrossRef] [PubMed]
26. Hajj, M.; Baghdadi, N.; Belaud, G.; Zribi, M.; Cheviron, B.; Courault, D.; Hagolle, O.; Charron, F. Irrigated grassland monitoring using a time series of TerraSAR-X and COSMO-SkyMed X-Band SAR data. *Remote Sens.* **2014**, *6*, 10002–10032. [CrossRef]
27. El Hajj, M.; Baghdadi, N.; Bazzi, H.; Zribi, M. Penetration analysis of SAR signals in the C and L bands for wheat, maize, and grasslands. *Remote Sens.* **2018**, *11*, 31. [CrossRef]
28. Nasrallah, A.; Baghdadi, N.; El Hajj, M.; Darwish, T.; Belhouchette, H.; Faour, G.; Darwich, S.; Mhawej, M. Sentinel-1 data for winter wheat phenology monitoring and mapping. *Remote Sens.* **2019**, *11*, 2228. [CrossRef]
29. Bazzi, H.; Baghdadi, N.; Fayad, I.; Zribi, M.; Belhouchette, H.; Demarez, V. Near real-time irrigation detection at plot scale using sentinel-1 data. *Remote Sens.* **2020**, *12*, 1456. [CrossRef]
30. Bazzi, H.; Baghdadi, N.; El Hajj, M.; Zribi, M. Potential of sentinel-1 surface soil moisture product for detecting heavy rainfall in the south of France. *Sensors* **2019**, *19*, 802. [CrossRef]
31. Le Page, M.; Jarlan, L.; El Hajj, M.M.; Zribi, M.; Baghdadi, N.; Boone, A. Potential for the detection of irrigation events on maize plots using sentinel-1 soil moisture products. *Remote Sens.* **2020**, *12*, 1621. [CrossRef]
32. Bazzi, H.; Baghdadi, N.; El Hajj, M.; Zribi, M.; Belhouchette, H. A Comparison of two soil moisture products S ^{2} MP and Copernicus-SSM over southern France. *IEEE J. Sel. Top. Appl. Earth Obs. Remote Sens.* **2019**, *12*, 3366–3375. [CrossRef]
33. Tiercelin, J.-R. *Traité D'irrigation*; Tec & Doc: Paris, France, 2006; ISBN 978-2-7430-0910-6.
34. Baghdadi, N.N.; El Hajj, M.; Zribi, M.; Fayad, I. Coupling SAR C-band and optical data for soil moisture and leaf area index retrieval over irrigated grasslands. *IEEE J. Sel. Top. Appl. Earth Obs. Remote Sens.* **2016**, *9*, 1229–1243. [CrossRef]
35. El Hajj, M.; Baghdadi, N.; Zribi, M.; Belaud, G.; Cheviron, B.; Courault, D.; Charron, F. Soil moisture retrieval over irrigated grassland using X-band SAR data. *Remote Sens. Environ.* **2016**, *176*, 202–218. [CrossRef]
36. Mérot, A. Analyse et Modélisation du Fonctionnement Biophysique et Décisionnel d'un Système Prairial Irrigué-Application aux Prairies Plurispécifiques de Crau En Vue de l'élaboration d'un Outil d'aide à la Décision. Ph.D. Thesis, Ecole Nationale Superieure Agronomique de Montpellier, Montpellier, France, September 2007.
37. Inglada, J.; Vincent, A.; Arias, M.; Tardy, B.; Morin, D.; Rodes, I. Operational high resolution land cover map production at the country scale using satellite image time series. *Remote Sens.* **2017**, *9*, 95. [CrossRef]
38. Cookmartin, G.; Saich, P.; Quegan, S.; Cordey, R.; Burgess-Allen, P.; Sowter, A. Modeling microwave interactions with crops and comparison with ERS-2 SAR observations. *IEEE Trans. Geosci. Remote Sens.* **2000**, *38*, 658–670. [CrossRef]
39. Mattia, F.; le Toan, T.; Picard, G.; Posa, F.I.; D'Alessio, A.; Notarnicola, C.; Gatti, A.M.; Rinaldi, M.; Satalino, G.; Pasquariello, G. Multitemporal c-band radar measurements on wheat fields. *IEEE Trans. Geosci. Remote Sens.* **2003**, *41*, 1551–1560. [CrossRef]

40. Del Frate, F.; Ferrazzoli, P.; Guerriero, L.; Strozzi, T.; Wegmuller, U.; Cookmartin, G.; Quegan, S. Wheat cycle monitoring using radar data and a neural network trained by a model. *IEEE Trans. Geosci. Remote Sens.* **2004**, *42*, 35–44. [CrossRef]
41. Baghdadi, N.; El Hajj, M.; Choker, M.; Zribi, M.; Bazzi, H.; Vaudour, E.; Gilliot, J.-M.; Ebengo, D. Potential of sentinel-1 images for estimating the soil roughness over bare agricultural soils. *Water* **2018**, *10*, 131. [CrossRef]
42. Baghdadi, N.; Zribi, M.; Loumagne, C.; Ansart, P.; Anguela, T. Analysis of TerraSAR-X data and their sensitivity to soil surface parameters over bare agricultural fields. *Remote Sens. Environ.* **2008**, *112*, 4370–4379. [CrossRef]

Publisher's Note: MDPI stays neutral with regard to jurisdictional claims in published maps and institutional affiliations.



© 2020 by the authors. Licensee MDPI, Basel, Switzerland. This article is an open access article distributed under the terms and conditions of the Creative Commons Attribution (CC BY) license (http://creativecommons.org/licenses/by/4.0/).